

Tension tuning of sound and heat transport in graphene

Hanqing Liu (✉ H.Liu-7@tudelft.nl)

Delft University of Technology

Martin Lee

Delft University of Technology

Makars Šiškins

Kavli Institute of Nanoscience, Delft University of Technology <https://orcid.org/0000-0003-4295-2221>

Herre van der Zant

Delft University of Technology <https://orcid.org/0000-0002-5385-0282>

Peter Steeneken

Delft University of Technology <https://orcid.org/0000-0002-5764-1218>

Gerard Verbiest

Delft University of Technology

Letter

Keywords:

Posted Date: May 6th, 2022

DOI: <https://doi.org/10.21203/rs.3.rs-1558097/v1>

License:   This work is licensed under a Creative Commons Attribution 4.0 International License.

[Read Full License](#)

1 Tension tuning of sound and heat transport in graphene

2 H. Liu¹, M. Lee², M. Šiškins^{1,2}, H. S. J. van der Zant², P. G. Steeneken^{1,2} and G. J. Verbiest¹

3 ¹*Department of Precision and Microsystems Engineering, Delft University of Technology*

4 ²*Kavli Institute of Nanoscience, Delft University of Technology*

5 **Heat transport by acoustic phonons in 2D materials is fundamentally different from that**
6 **in 3D crystals¹⁻⁴ because the out-of-plane phonons propagate in a unique way that strongly**
7 **depends on tension and bending rigidity. Since in-plane and out-of-plane phonon baths are**
8 **decoupled, initial studies suggested they provide independent pathways for heat transport**
9 **and storage in 2D materials^{5,6}. Here, we induce tension in freestanding graphene membranes**
10 **by electrostatic force, and use optomechanical techniques to demonstrate that it can change**
11 **the rate of heat transport by as much as 33%. Using a ballistic Debye model, we account for**
12 **these observations and extract the average bending rigidity of the flexural acoustic phonons,**
13 **which increases approximately linearly with the membrane's areal mass density, in contrast**
14 **to the cubic dependence seen in bulk structures. Thus, we not only elucidate phononic heat**
15 **transport mechanisms in suspended 2D materials, but also provide a promising route for**
16 **controlling nanoscale heat transport by tension.**

17 Although in most bulk materials the propagation speed of different types of acoustic phonons
18 is of similar magnitude, the situation is vastly different in 2D materials^{7,8}. In these atomically
19 thin materials, in-plane phonons have a propagation speed that is determined by the atomic bond
20 stiffnesses, whereas out-of-plane flexural phonons, exhibit a speed that is dominated by tension

21 and can be more than an order of magnitude smaller⁹⁻¹², while also showing a unique quadratic
22 dispersion relation.

23 Evidence for the importance of these speed differences on the phononic heat transport in 2D ma-
24 terials was provided by theoretical analysis¹³ and by the observation of two distinct thermal time
25 constants in graphene membranes, of which the longest, τ , is a probe for studying heat transport
26 by the relatively slow flexural phonons^{6,14}. To understand heat propagation via these different in-
27 plane and out-of-plane phononic channels in 2D materials, studies of the role of flexural phonons
28 are essential. Yet, unlike the thermal conductivity of 2D materials which has been well character-
29 ized by Raman microscopy^{15,16}, a microscopic picture of how the rate of heat transport is related
30 to the properties of flexural phonons remains elusive, as it requires a methodology for measuring
31 their effect on temperature variations in suspended 2D materials with nanosecond resolution.

32 In this letter, we experimentally determine the heat transport rate in graphene drum resonators and
33 demonstrate its tunability by tension. We first determine the tension and effective mass of four
34 graphene resonators using high-frequency optomechanical technique¹⁷ by measuring the depen-
35 dence of the mechanical resonance frequency on gate voltage induced electrostatic forces. Then,
36 by applying the same technique in low frequency domain, we determine the gate tunability of the
37 thermal time constant and effective thermal expansion coefficients of the membranes. Finally, by
38 relating these measurements to a model for phononic heat transport, we characterize the ballistic
39 transport and boundary scattering of phonons, the effect of graphene's bending rigidity on 2D heat
40 transport and the relative thermal expansion contributions of flexural and in-plane phonons.

41 We present measurements on four CVD-grown double-layer graphene drum resonators D1–D4
 42 (see fabrication in Methods). Resonators D1 and D2 have radii of $r = 2.5 \mu\text{m}$ and D3 and D4
 43 have radii of $r = 5 \mu\text{m}$. Fig. 1a-b shows a schematic illustration and an optical microscope image
 44 of a drum resonator. The cavity depth d_1 is 245 nm and the thickness of the remaining unetched
 45 SiO_2 layer at the bottom of the cavity d_2 is 40 nm. The surface profile measured by atomic force
 46 microscopy (AFM) indicates an initial downward deflection d_0 of the membrane, resulting from
 47 sidewall adhesion at the edge of the membrane¹⁸ (see Fig. 1c). We measure the motion of the
 48 membrane using the interferometer depicted in Fig. 1d (see Methods and SI section 1 for details).
 49 Figure. 1e shows the measured motion amplitude z_ω of device D1 at $V_g = 0 \text{ V}$ over the frequency
 50 range from 0.1 to 100 MHz. We extract the resonance frequency ω_0 and quality factor Q by fit-
 51 ting the measured data to a harmonic oscillator model (Fig. 1f). For device D1 this results in
 52 $\omega_0/(2\pi) = 25.49 \text{ MHz}$ and $Q = 43.25$. Around 1 MHz, we observe an additional broad peak in the
 53 imaginary part of the frequency response (Fig. 1g). We identify this peak as the thermal peak of
 54 resonator, since it is only there when driving the membrane optothermally¹⁷. Following literature⁶,
 55 below mechanical resonance, the displacement z_ω is a measure of the displacement due to thermal
 56 expansion that is delayed with respect to the laser power as a consequence of the time it takes to
 57 increase the membrane temperature by laser heating. Around the thermal peak in Fig. 1g, z_ω is
 58 given by:

$$z_\omega = \frac{C_{\text{slow}}}{1 + i\omega\tau} + C_{\text{fast}}, \quad (1)$$

59 where τ is the thermal time constant, and C_{slow} and C_{fast} quantify the device's effective thermal
 60 expansion coefficients due to the out-of-plane and in-plane phonons, respectively⁶. We extract

61 these parameters by fitting the real and imaginary parts of the measured z_ω with equation 1, as
 62 depicted in Fig. 1g. Here, the thermal peak is located at 1.23 MHz, corresponding to $\tau = (2\pi \times$
 63 $1.23 \text{ MHz})^{-1} = 129 \text{ ns}$.

64 To determine the tension n in the drum, we measure its resonance frequency ω_0 as a function
 65 of applied electrostatic gate voltage V_g (see Fig. 1a). The voltage V_g generates an electrostatic
 66 force, pulling the drum down thereby inducing tension. Figure. 2a shows $\omega_0/(2\pi)$ against V_g for
 67 all devices from -4 V to 4 V . The typical W-shaped curves show both electrostatic softening and
 68 tension hardening (indicated by arrows), as often observed in electrostatic gate-tuning of graphene
 69 NEMS¹⁹. Following literature¹⁹, we model the frequency tuning of the drum resonator from con-
 70 tinuum mechanics with:

$$\omega_0(V_g) = \sqrt{\frac{1}{m_{\text{eff}}} \left[\frac{2\pi Et\epsilon_0}{1-v^2} + \frac{8\pi Et}{(1-v^2)r^2} z_g^2 - \frac{1}{2} \frac{\partial^2 C_g}{\partial z_g^2} V_g^2 \right]}, \quad (2)$$

71 in which ϵ_0 is the built-in strain, m_{eff} is the modal mass of the fundamental mode of the circular
 72 membrane resonator with a theoretical value $m_{\text{eff,th}} = 0.271\pi r^2 \rho_g$ where ρ_g is the mass density of
 73 double-layer graphene, C_g is the capacitance between membrane and bottom gate, and the deriva-
 74 tive $\frac{\partial^2 C_g}{\partial z_g^2}$ quantifies the electrostatic softening. The 2D Young's modulus $Et \approx 175.39 \text{ N/m}$ and
 75 Poisson ratio $v = 0.16$ were determined via AFM indentation²⁰ (see SI section 1). The center
 76 deflection z_g can be expressed²¹ as $\epsilon_0 r^2 V_g^2 / (8g_0^2 n_0)$, where $n_0 = Et\epsilon_0 / (1-v)$ is the pretension,
 77 ϵ_0 is the permittivity of vacuum, and g_0 is the effective gap between the drum and the electrostatic
 78 gate. We fit the measured V_g dependence of ω_0 with equation (2) (black lines in Fig. 2a) to extract
 79 n_0 , m_{eff} and $\frac{\partial^2 C_g}{\partial z_g^2}$ for each device (listed in Table 1).

80 The extracted initial tension n_0 ranging between 0.18 to 0.34 N/m is in agreement with the lit-
81 erature values reported for graphene NEMS^{19,21–23}, and m_{eff} of 0.39 to 1.06×10^{-16} kg is larger
82 than the mass expected for double-layer graphene, which is attributed to polymer residues left after
83 fabrication^{22,24}. The values for $\frac{\partial^2 C_g}{\partial z_g^2}$ are close to the theoretical estimate $0.542\varepsilon_0\pi r^2/g_0^3$ from the
84 geometry of the capacitor²⁵. The excellent agreement between the fit and measured dependence
85 of ω_0 on gate voltage (Fig. 2a) allows to extract the membrane tension n at each value of V_g and
86 corresponding center deflection z_g , using the equation¹⁹ $n = n_0(1 + 4z_g^2/r^2)$.

87 Besides the changes in the resonance frequency ω_0 , we also observe that the measured thermal
88 time constant τ decreases with V_g for all devices (dots, Fig. 2b–2d), as much as 33%. To shed
89 light on this observation, we use a phononic model to assess the transient thermal conduction in the
90 membrane¹³. We assume in the model that the transport of flexural acoustic phonons in the mem-
91 brane is ballistic, since their mean free paths are much longer than the radius r of membranes²⁶,
92 while using a scattering model²⁷ (see Methods and Fig. S1) to capture the tension dependent
93 phonon transport across the kink at the edge of the membrane (Fig. 1c). This results in the follow-
94 ing function:

$$\tau = \frac{r}{2 \sum_j \bar{w}_{1z \rightarrow 2j} c_z}, j = l, t, z, \quad (3)$$

95 in which $\bar{w}_{1z \rightarrow 2j}$ is the probability that a flexural phonon on the suspended part of the graphene
96 (subscript 1) is transmitted across the membrane edge and becomes a phonon of type j on the
97 supported part of the graphene (subscript 2), where j can either be a flexural phonon ($j = z$), or
98 a longitudinal or transverse in-plane phonon ($j = l, t$). The scattering probability $\bar{w}_{1z \rightarrow 2j}$ depends
99 both on tension n and on the speed of sound c_z of flexural phonons. The dispersion relation for

100 flexural phonons is given by $\omega_q = \sqrt{(\kappa q^4 + nq^2)/(\eta\rho_g)}$ (ref.²⁸), where q is the wavenumber, κ is
 101 the bending rigidity of the membrane, and $\eta = m_{\text{eff}}/(0.271\pi r^2\rho_g)$ is the normalized areal mass of
 102 the membrane (see Table 1). From the dispersion relation the speed of sound for flexural phonons
 103 can be found using $c_z = \frac{\partial\omega_q}{\partial q}$.

104 In practice, flexural phonons with frequencies up to the Debye frequency ω_{qd} , will contribute to
 105 the heat transport and thermal time constant τ . To account for this (see Fig. 3a), we integrate
 106 over the Bose-Einstein distribution using the phonon speed distribution $c_z(\omega_q, n)$ to calculate the
 107 specific heat spectral density $C_{v,\omega}^z(\omega_q, n)$ of flexural phonons (Debye model); then, knowledge of
 108 the tension n and speed of sound c_z allows to solve equation (3) and determine $\tau(\omega_q, n)$; finally
 109 a weighted average over the contribution of phonons at each frequency ω_q to the thermal time
 110 constant $\tau(n)$ is determined using $1/\tau(n) = \int_0^{\omega_{qd}} C_{v,\omega}^z(\omega_q, n)/(C_v^z(n)\tau(\omega_q, n))d\omega_q$, where the total
 111 specific heat due to flexural phonons is determined using $C_v^z(n) = \int_0^{\omega_{qd}} C_{v,\omega}^z(\omega_q, n)d\omega_q$ ^{28,29}. More
 112 details about the scattering and Debye models can be found in SI section 3 and 4.

113 From the presented measurements, all parameters in the above model (green color in Fig. 3a) can
 114 be determined. Only the bending rigidity of graphene is not measured, which especially affects
 115 high frequency (\sim THz) flexural phonons near the Debye frequency ω_{qd} (Fig. S4). We therefore
 116 use the bending rigidity κ as a fit parameter, to match the modelled τ to the experimental values
 117 for all devices D1–D4 (see Fig. 2b–2e). The value of κ varies in a broad range, from 0.6 to
 118 9.4 eV roughly, which is comparable to values reported in literature^{30,31}. Interestingly, κ is roughly
 119 proportional to the normalized areal mass η of the membranes (see Fig. 3b), indicating that polymer

120 residues not only affect the mechanical properties of the membrane, but also seem to play an
 121 important role in the heat transport by increasing the membrane's bending rigidity.

122 Let us now focus on the amplitudes C_{fast} and C_{slow} in equation (1), which measure the magnitude of
 123 the thermal expansion of the in-plane and flexural phonons, respectively (as indicated in Fig. 1g).

124 The measured ratio $|C_{\text{fast}}/C_{\text{slow}}|$ is approximately proportional to the relative temperature increase
 125 of both phonon baths⁶ and increases with tension n from 0.02 to 0.23 (Fig. 3c, points). Since

126 the temperature increase depends both on the absorbed laser power and the cooling rate by heat

127 transport, we have $|C_{\text{fast}}/C_{\text{slow}}| = \gamma \frac{(\tau_l/C_v^l + \tau_t/C_v^t)}{\tau/C_v^z}$, where $\gamma = P_{\text{abs}}^{l,t}/P_{\text{abs}}^z$ is the power absorption

128 ratio between in-plane and flexural phonons (see SI section 5 for derivation). By applying the

129 same procedure as for τ , we calculate τ_l and τ_t for the in-plane phonons using their specific heats

130 C_v^l and C_v^t (see Fig. S3). From these values we determine the ratio $|C_{\text{fast}}/C_{\text{slow}}|$ from the model and

131 use γ to fit it to the measured thermal expansion ratio, obtaining a single value of γ for each device

132 (listed in Table 1). As shown in Fig. 3c the model accurately captures the tension dependence of

133 the ratio $|C_{\text{fast}}/C_{\text{slow}}|$ for all devices. The observed increase in $|C_{\text{fast}}/C_{\text{slow}}|$ is a consequence of

134 c_z increase with increasing tension, which reduces τ such that C_{slow} decreases¹⁰. From γ , we can

135 calculate the percentage ξ of optical power that is converted into flexural phonons, expressed as

136 $\xi = P_{\text{abs}}^z / (P_{\text{abs}}^{l,t} + P_{\text{abs}}^z) \times 100\% = (1 + \gamma)^{-1} \times 100\%$. As Fig. 3d shows, ξ rapidly decreases from

137 43.7% to less than 15% when the normalized areal mass η increases.

138 In Figs. 2 and 3c, we show that the presented model can capture the tension dependence of the

139 resonance frequency ω_0 , thermal time constant τ and thermal expansion ratio $|C_{\text{fast}}/C_{\text{slow}}|$ very

140 well for all devices, using only κ and γ as fit parameter. The extracted κ shows large variation
 141 between our devices (Fig. 3b) that is correlated to the areal mass density η . Since the devices
 142 are fabricated identically, we attribute the differences to variations in residues on and between the
 143 double CVD graphene layers. These residues affect acoustic phonon transport in three different
 144 ways. First, residues decrease ξ , the relative optical power absorbed by flexural phonons (Fig.
 145 3d), and thus decrease their contribution to the thermal expansion of graphene^{32,33}. Second, the
 146 effective mass of the membrane and thus of the flexural phonons, quantified by the normalized areal
 147 mass η , is increased (Table 1). Third, the bending rigidity κ increases (Fig. 3b). This results in the
 148 observed linear relation between κ and η which is somewhat surprising, since for a bulk material κ
 149 is expected to exhibit cubic scaling with thickness³⁴. However, if the interlayer shear interaction
 150 between the layers is weak, a linear dependence is predicted to occur³⁵. For high frequency (\sim THz)
 151 phonons, the variations in bending rigidity have little effect on the dispersion relation $\omega_q(q)$ for
 152 all devices D1–D4 (Fig. 4a, left panel). In contrast, the specific heat spectral density $C_{v,\omega}^z(\omega_q)$
 153 still shows significant device-to-device variations (Fig. 4a, right panel), that are held responsible
 154 for the measured variations in the heat transport rate τ . More details about how κ and η affect
 155 $\omega_q(q)$ and $C_{v,\omega}^z(\omega_q)$ can be found in SI section 4. For low frequency (MHz) flexural phonons,
 156 the situation is completely different. The resonance frequency of the graphene membranes can
 157 be understood as a standing wave of a flexural acoustic phonons and is thus proportional to the
 158 ratio of the speed of sound c_z and the membrane radius, such that κ does not play an important
 159 role. For MHz frequencies, c_z is thus fully determined by n and η , in-line with all experimental
 160 graphene resonators reported in the literature^{19,21}. We estimate the cross-over frequency ω_{qc} where

161 the phonon frequency $\omega_q(q)$ shows a transition from tension n - dominated to bending rigidity κ -
162 dominated regime, at around 84.8, 52.6, 174.4 and 422.7 GHz for devices D1–D4, respectively
163 (Fig. S4b). By measuring the resonance frequencies we obtain information on the tension and
164 mass of the membrane, that can be used to determine the low frequency phonon dispersion, while
165 with the thermal time constant and thermal expansion ratio we can estimate the bending rigidity
166 that is essential for the high frequency phonon dispersion. Thus the measurements and model allow
167 us to assess the acoustic phonon dispersion from the MHz to the THz regime.

168 For each of our devices, tension n tunes the heat transport rate in three different ways: speed of
169 sound c_z , the specific heat spectral density $C_{v,\omega}^z(\omega_q)$, and the phonon scattering rate as expressed
170 in equation (3). Since n only affects the dispersion relation of low frequency (MHz) phonons,
171 its impact on the thermal time constant τ through the speed of sound c_z and heat capacitance
172 $C_{v,\omega}^z(\omega_q)$ is limited (Fig. S5f and i). Therefore, the observed decrease of thermal time constant τ
173 in Fig. 2 is attributed to the enhanced acoustic impedance matching between the flexural phonons
174 on the suspended membrane and the in-plane phonons on the supported membrane, leading to
175 faster heat dissipation. This conclusion is supported by the calculations in Fig. 4b that are based
176 on the experimental device parameters and data (green points) obtained for device D3. It shows
177 that as n increases from 0.1 to 1000 N/m, τ decreases from $\sim 1 \mu\text{s}$ to less than 0.3 ns, attributed
178 both to the increase of the phonon transmission probability $\bar{w}_{1z \rightarrow 2j}$ of flexural phonons and to the
179 increased speed of sound ($c_z \approx \sqrt{n/(\eta\rho_g)}$ for $n \gg \kappa q^2$). More details about the influence of κ
180 on τ can be found in SI section 4. Note that the extremely high tension $n = 1000 \text{ N/m}$ is only
181 for the discussion and cannot be physically realised in graphene membranes. For small tensions

182 the thermal time constant is mainly limited by the phonon transmission probability and bending
183 rigidity, whereas for high tensions ($n > 100$ N/m) it is mainly the speed of phonons and the distance
184 they have to travel that limit heat conduction. Such low τ is comparable to the propagation time
185 of heat flux from the centre to the boundary of membrane^{17,36}, given by $\tau = r^2 / (5\alpha_{td})$ where α_{td}
186 is the thermal diffusivity of the membrane, which also sets a limit on the tunable acoustic phonon
187 transport by tension. Understanding this limit is important for proposed applications in the field
188 of 2D phononics, such as switchable thermal transistors, ultra-sensitive thermal logic gates, and
189 reconfigurable phononic memories^{37,38}.

190 Recent observations revealed that acoustic phonons play an important role in macroscopic quantum
191 states in 2D materials, such as superconductivity and ferromagnetism^{39,40}. We anticipate that the
192 changes in the dispersion relation of flexural phonons found in this work could provide crucial in-
193 sight into these quantum phase transitions, especially the transition temperature and doping effects
194 in magic-angle twisted bilayer/trilayer graphene⁴¹ and multilayer rhombohedral graphene⁴².

195 In conclusion, we measured nanosecond-scale heat transport in suspended graphene drums and
196 presented experimental demonstration of its tunability with in-plane tension. Using a Debye scat-
197 tering model of acoustic phonons, we present a microscopic picture of heat transport in suspended
198 graphene membranes, where bending rigidity and tension dominate the flexural dispersion rela-
199 tion for THz and MHz frequency phonons, respectively. The gained insight not only advances our
200 fundamental understanding of acoustic phonons in 2D materials, but also enables pathways for
201 controlled and optimized thermal management in 2D-based phononic, thermoelectric, electronic

202 and quantum devices.

203 **References**

- 204 1. Chen, S. *et al.* Thermal conductivity of isotopically modified graphene. *Nat. Mater.* **11**, 203–
205 207 (2012).
- 206 2. Lindsay, L., Broido, D. & Mingo, N. Flexural phonons and thermal transport in graphene.
207 *Phys. Rev. B* **82**, 115427 (2010).
- 208 3. Wang, R. *et al.* Distinguishing optical and acoustic phonon temperatures and their energy
209 coupling factor under photon excitation in nm 2D materials. *Adv. Sci.* **7**, 2000097 (2020).
- 210 4. Lee, S., Broido, D., Esfarjani, K. & Chen, G. Hydrodynamic phonon transport in suspended
211 graphene. *Nat. Commun.* **6**, 1–10 (2015).
- 212 5. Sullivan, S. *et al.* Optical generation and detection of local nonequilibrium phonons in sus-
213 pended graphene. *Nano lett.* **17**, 2049–2056 (2017).
- 214 6. Dolleman, R. J., Verbiest, G. J., Blanter, Y. M., van der Zant, H. S. & Steeneken, P. G.
215 Nonequilibrium thermodynamics of acoustic phonons in suspended graphene. *Phys. Rev. Res*
216 **2**, 012058 (2020).
- 217 7. Taheri, A., Pisana, S. & Singh, C. V. Importance of quadratic dispersion in acoustic flexural
218 phonons for thermal transport of two-dimensional materials. *Phys. Rev. B* **103**, 235426 (2021).

- 219 8. Cepellotti, A. *et al.* Phonon hydrodynamics in two-dimensional materials. *Nat. Commun.* **6**,
220 1–7 (2015).
- 221 9. Mariani, E. & Von Oppen, F. Flexural phonons in free-standing graphene. *Phys. Rev. Lett.*
222 **100**, 076801 (2008).
- 223 10. Castro, E. V. *et al.* Limits on charge carrier mobility in suspended graphene due to flexural
224 phonons. *Phys. Rev. Lett.* **105**, 266601 (2010).
- 225 11. Bonini, N., Garg, J. & Marzari, N. Acoustic phonon lifetimes and thermal transport in free-
226 standing and strained graphene. *Nano lett.* **12**, 2673–2678 (2012).
- 227 12. Tornatzky, H., Gillen, R., Uchiyama, H. & Maultzsch, J. Phonon dispersion in MoS₂. *Phys.*
228 *Rev. B* **99**, 144309 (2019).
- 229 13. Vallabhaneni, A. K., Singh, D., Bao, H., Murthy, J. & Ruan, X. Reliability of raman mea-
230 surements of thermal conductivity of single-layer graphene due to selective electron-phonon
231 coupling: A first-principles study. *Phys. Rev. B* **93**, 125432 (2016).
- 232 14. Dolleman, R. J. *et al.* Transient thermal characterization of suspended monolayer MoS₂. *Phys.*
233 *Rev. Mat.* **2**, 114008 (2018).
- 234 15. Ghosh, D. *et al.* Extremely high thermal conductivity of graphene: Prospects for thermal
235 management applications in nanoelectronic circuits. *Appl. Phys. Lett.* **92**, 151911 (2008).
- 236 16. Balandin, A. A. *et al.* Superior thermal conductivity of single-layer graphene. *Nano lett.* **8**,
237 902–907 (2008).

- 238 17. Dolleman, R. J. *et al.* Optomechanics for thermal characterization of suspended graphene.
239 *Phys. Rev. B* **96**, 165421 (2017).
- 240 18. Bunch, J. S. *et al.* Impermeable atomic membranes from graphene sheets. *Nano lett.* **8**, 2458–
241 2462 (2008).
- 242 19. Chen, C. *et al.* Performance of monolayer graphene nanomechanical resonators with electrical
243 readout. *Nat. Nanotechnol.* **4**, 861–867 (2009).
- 244 20. Šiškins, M. *et al.* Sensitive capacitive pressure sensors based on graphene membrane arrays.
245 *Microsyst. Nanoeng.* **6**, 1–9 (2020).
- 246 21. Weber, P., Guttinger, J., Tsioutsios, I., Chang, D. E. & Bachtold, A. Coupling graphene me-
247 chanical resonators to superconducting microwave cavities. *Nano lett.* **14**, 2854–2860 (2014).
- 248 22. Will, M. *et al.* High quality factor graphene-based two-dimensional heterostructure mechani-
249 cal resonator. *Nano lett.* **17**, 5950–5955 (2017).
- 250 23. Zhang, X. *et al.* Dynamically-enhanced strain in atomically thin resonators. *Nat. Commun.*
251 **11**, 1–9 (2020).
- 252 24. Miao, T., Yeom, S., Wang, P., Standley, B. & Bockrath, M. Graphene nanoelectromechanical
253 systems as stochastic-frequency oscillators. *Nano lett.* **14**, 2982–2987 (2014).
- 254 25. Šiškins, M. *et al.* Magnetic and electronic phase transitions probed by nanomechanical res-
255 onators. *Nat. Commun.* **11**, 1–7 (2020).

- 256 26. Fugallo, G. *et al.* Thermal conductivity of graphene and graphite: collective excitations and
257 mean free paths. *Nano lett.* **14**, 6109–6114 (2014).
- 258 27. Dolleman, R. J., Blanter, Y. M., van der Zant, H. S. J., Steeneken, P. G. & Verbiest, G. J.
259 Phonon scattering at kinks in suspended graphene. *Phys. Rev. B* **101**, 115411 (2020).
- 260 28. Nihira, T. & Iwata, T. Temperature dependence of lattice vibrations and analysis of the specific
261 heat of graphite. *Phys. Rev. B* **68**, 134305 (2003).
- 262 29. Singh, D., Murthy, J. Y. & Fisher, T. S. Mechanism of thermal conductivity reduction in
263 few-layer graphene. *J. Appl. Phys.* **110**, 044317 (2011).
- 264 30. Han, E. *et al.* Ultrasoft slip-mediated bending in few-layer graphene. *Nat. Mater.* **19**, 305–309
265 (2020).
- 266 31. Wei, Y., Wang, B., Wu, J., Yang, R. & Dunn, M. L. Bending rigidity and gaussian bending
267 stiffness of single-layered graphene. *Nano lett.* **13**, 26–30 (2013).
- 268 32. Mercado, E., Anaya, J. & Kuball, M. Impact of polymer residue level on the in-plane thermal
269 conductivity of suspended large-area graphene sheets. *ACS Appl. Mater. Interfaces* **13**, 17910–
270 17919 (2021).
- 271 33. Pettes, M. T., Jo, I., Yao, Z. & Shi, L. Influence of polymeric residue on the thermal conduc-
272 tivity of suspended bilayer graphene. *Nano lett.* **11**, 1195–1200 (2011).
- 273 34. Lindahl, N. *et al.* Determination of the bending rigidity of graphene via electrostatic actuation
274 of buckled membranes. *Nano lett.* **12**, 3526–3531 (2012).

- 275 35. Wang, G. *et al.* Bending of multilayer van der Waals materials. *Phys. Rev. Lett.* **123**, 116101
276 (2019).
- 277 36. Dolleman, R. J., Davidovikj, D., van der Zant, H. S. J. & Steeneken, P. G. Amplitude cali-
278 bration of 2D mechanical resonators by nonlinear optical transduction. *Appl. Phys. Lett.* **111**,
279 253104 (2017).
- 280 37. Maldovan, M. Sound and heat revolutions in phononics. *Nature* **503**, 209–217 (2013).
- 281 38. Balandin, A. A. Phononics of graphene and related materials. *ACS nano* **14**, 5170–5178
282 (2020).
- 283 39. Liu, X. & Hersam, M. C. 2D materials for quantum information science. *Nat. Rev. Mater.* **4**,
284 669–684 (2019).
- 285 40. Chou, Y.-Z., Wu, F., Sau, J. D. & Sarma, S. D. Acoustic-phonon-mediated superconductivity
286 in rhombohedral trilayer graphene. *Phys. Rev. Lett.* **127**, 187001 (2021).
- 287 41. Cao, Y. *et al.* Unconventional superconductivity in magic-angle graphene superlattices. *Nature*
288 **556**, 43–50 (2018).
- 289 42. Shi, Y. *et al.* Electronic phase separation in multilayer rhombohedral graphite. *Nature* **584**,
290 210–214 (2020).
- 291 43. Cai, W. *et al.* Thermal transport in suspended and supported monolayer graphene grown by
292 chemical vapor deposition. *Nano Lett.* **10**, 1645–1651 (2010).

- 293 44. Li, Q.-Y. *et al.* Measurement of specific heat and thermal conductivity of supported and
294 suspended graphene by a comprehensive raman optothermal method. *Nanoscale* **9**, 10784–
295 10793 (2017).
- 296 45. Atalaya, J., Isacson, A. & Kinaret, J. M. Continuum elastic modeling of graphene resonators.
297 *Nano lett.* **8**, 4196–4200 (2008).

298 **Methods**

299 **Sample fabrication.** We pattern circular cavities with a depth of 240 nm using reactive ion etching
300 into a Si/SiO₂ chip. We pattern Ti/Au electrodes (5/60 nm) on the chip firstly along with the e-beam
301 markers, which are then used to define the cavities. The cavity depth is less than the SiO₂ thickness
302 of 285 nm to prevent an electrical short-circuit between the Si electrode and the suspended drums.
303 We subsequently transfer large-scale CVD graphene over the cavities. This double-layer graphene
304 is fabricated by stamping one monolayer CVD graphene on top of another one, where an extra
305 layer of polymethyl methacrylate (PMMA) is attached on each graphene layer. Finally, we remove
306 the PMMA by annealing the devices in a furnace at a pressure of 500 Torr with a constant flow of
307 0.5 SLPM of an inert dry gas (Ar or N₂) at a temperature of 300 °C. After 30 min annealing, most
308 of the PMMA has been evaporated.

309 **Optothermal drive.** To measure ω_0 , τ , C_{fast} , and C_{slow} in the graphene drums, we use an interfer-
310 ometer to actuate and detect its motion. An intensity modulated blue laser ($\lambda = 405$ nm) irradiates
311 the suspended drum resulting in a periodic heat flux³⁶. The heat flux results in a motion of the drum
312 due to the thermal expansion force. A red laser ($\lambda = 633$ nm) is used to detect the out-of-plane

313 motion of the graphene drum. Also, this technique allows to measure the thermal characteriza-
314 tions of suspended devices without the need to calibrate the spotsize and intensity of laser as in
315 the Raman based methods^{43,44}. All measurements are performed at room temperature inside a vac-
316 uum chamber at 10^{-6} mbar. A vector network analyzer (VNA) modulates the intensity of a blue
317 laser at frequency ω to optothermally actuate a resonator while it analyzes the resulting intensity
318 modulation of the red laser caused by the mechanical response of the same resonator. The red and
319 blue laser powers used are 1.2 and 0.13 mW respectively, where it was verified that the resonators
320 vibrate in the linear regime and the temperature increase due to self-heating was negligible¹⁷.

321 **Scattering model of acoustic phonons.** We develop this model at the sidewall between the sus-
322 pended (domain 1) and supported (domain 2) graphene to evaluate thermal time constant τ (see
323 diagram in Fig. S1a). For incoming flexural phonons (defined as mode $1z$), the transmission prob-
324 ability $w_{1z \rightarrow 2j}(j = l, t, z)$ can be calculated as a function of the incident angle θ_{1z} (see Fig. S1b
325 for details). Here, $c_l = 21.6$ km/s and $c_t = 16$ km/s are extracted from the linear dispersion of
326 in-plane phonons in graphene, using⁴⁵ Lamé parameters $\lambda = 48$ J/m² $\mu = 144$ J/m². The total
327 transmission coefficient $\bar{w}_{1z \rightarrow 2j}$ is then obtained by integrating $w_{1z \rightarrow 2j}$ over all incidence angles
328 from $-\pi/2$ to $\pi/2$. We also assume kink angle $\beta = 90^\circ$ at the edge of the membrane. Wrinkles
329 and ripples in membrane surface can be regarded as kinks with a tiny β , of which contributions to
330 the heat transport can be negligible since τ reduces dramatically as β decreases²⁷.

331 **Acknowledgements** P.G.S. and G.J.V. acknowledges support by the Dutch 4TU federation for the Plantenna
332 project. H.L. acknowledges the financial support from China Scholarship Council. M.L., M.Š., H.S.J.v.d.Z.

Table 1: Characteristics of devices D1–D4. Radius r , effective gap g_0 , pretension n_0 , effective mass m_{eff} , normalized areal mass η , the second derivative of the capacitance with respect to the electrostatic deflection $\frac{\partial^2 C_g}{\partial z_g^2}$, bending rigidity κ as well as the relative power absorption γ in the ratio of thermal expansion coefficients.

device	r	g_0	n_0	m_{eff}	η	$\frac{\partial^2 C_g}{\partial z_g^2}$	κ	γ
	(μm)	(nm)	(N/m)	($\times 10^{-16}\text{kg}$)		(mF m $^{-2}$)	(eV)	
D1	2.5	212	0.24	0.50	19.40	6.56	3.8	8.18
D2	2.5	237	0.34	0.96	37.10	9.12	9.4	6.90
D3	5	227	0.21	1.06	10.36	34.75	2.2	3.26
D4	5	237	0.18	0.39	3.80	30.35	0.6	1.29

333 and P.G.S. acknowledge funding from the European Union’s Horizon 2020 research and innovation pro-
334 gram under grant agreement number 881603. We thank Applied Nanolayers (ANL) for transferring CVD
335 graphene on the chips.

336 **Competing Interests** The authors declare that they have no competing financial interests.

337 **Correspondence** Correspondence and requests for materials should be addressed to H. Liu (email: H.Liu-
338 7@tudelft.nl) and G. J. Verbiest (email: G.J.Verbiest@tudelft.nl).

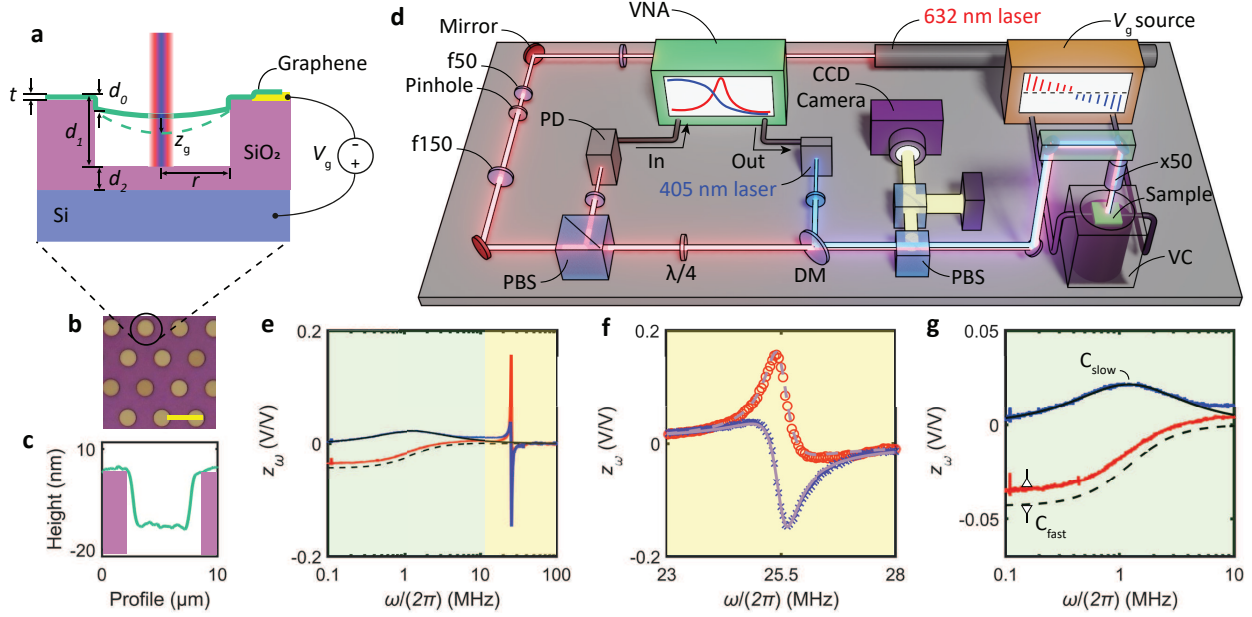


Fig. 1: Graphene membrane characterization. **a**, Schematic of a graphene drum of radius r over a cavity of depth d_1 in a SiO_2/Si substrate irradiated by lasers. The graphene has a sidewall of length d_0 into the cavity. The effective electrostatic gap is expressed as $g_0 = d_1 - d_0 + d_2/\epsilon_{\text{SiO}_2}$. The voltage V_g pulls the drum down by z_g , increasing its tension. **b**, Optical image of the drums with a scale bar of $10 \mu\text{m}$. **c**, Atomic force microscope line trace over a suspended drum indicates a downward deformation of drum. **d**, Interferometric setup. The sample is placed inside a vacuum chamber (VC). The blue (405 nm) laser is intensity modulated by a vector network analyzer (VNA) to actuate the resonator. Intensity variations of the reflected red (633 nm) laser caused by resonator motion, are measured by photodiode (PD) and recorded with the VNA. PBS: polarized beam splitter; DM: dichroic mirror. **e**, Frequency response of device D1, including real (red) and imaginary (blue) parts of the motion z_ω . **f**, Fits of z_ω (lines) to equation (1) to obtain the resonance frequency ω_0 . **g**, Fits of equation (1) to z_ω near the thermal peak (black solid and dashed lines) provide the thermal time constant τ and thermal expansion C_{fast} and C_{slow} of the resonator.

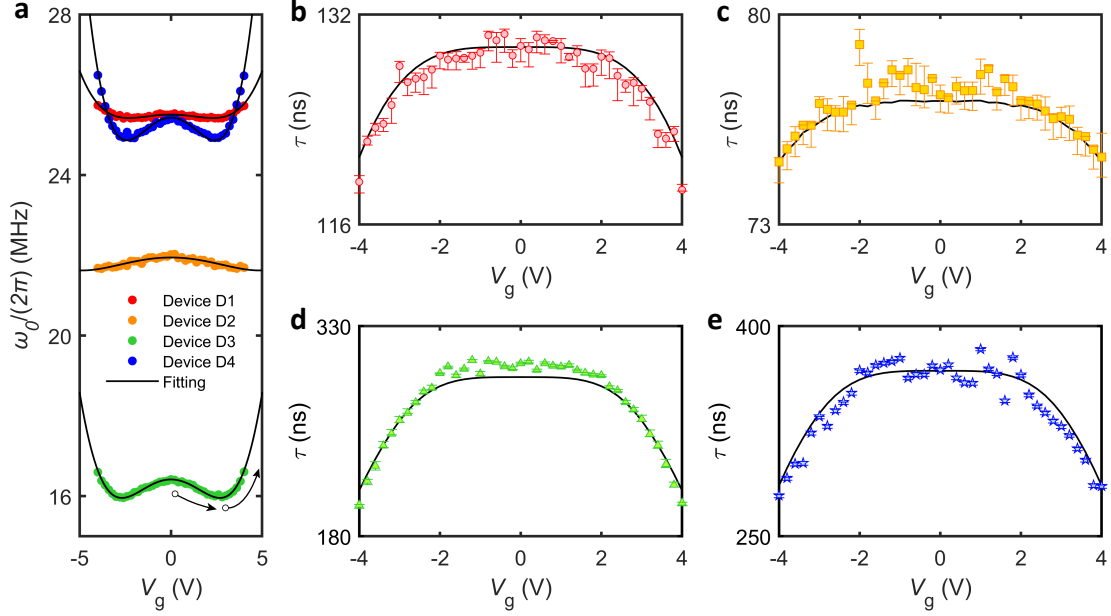


Fig. 2: Tuning thermodynamic properties of graphene drum devices with gate voltage. **a**, Solid dots: resonance frequency ω_0 versus gate voltage V_g measured in devices D1–D4; drawn lines: fits based on equation (2); arrows indicate the modulation from the capacitive softening regime to the tension dominated (hardening) regime. **b–e**, Points: thermal time constant τ versus V_g measured in devices D1–D4, respectively; solid lines: fits to data using the Debye-scattering model; error bars are from the fits to the measured thermal peaks as plotted in Fig. 1g.

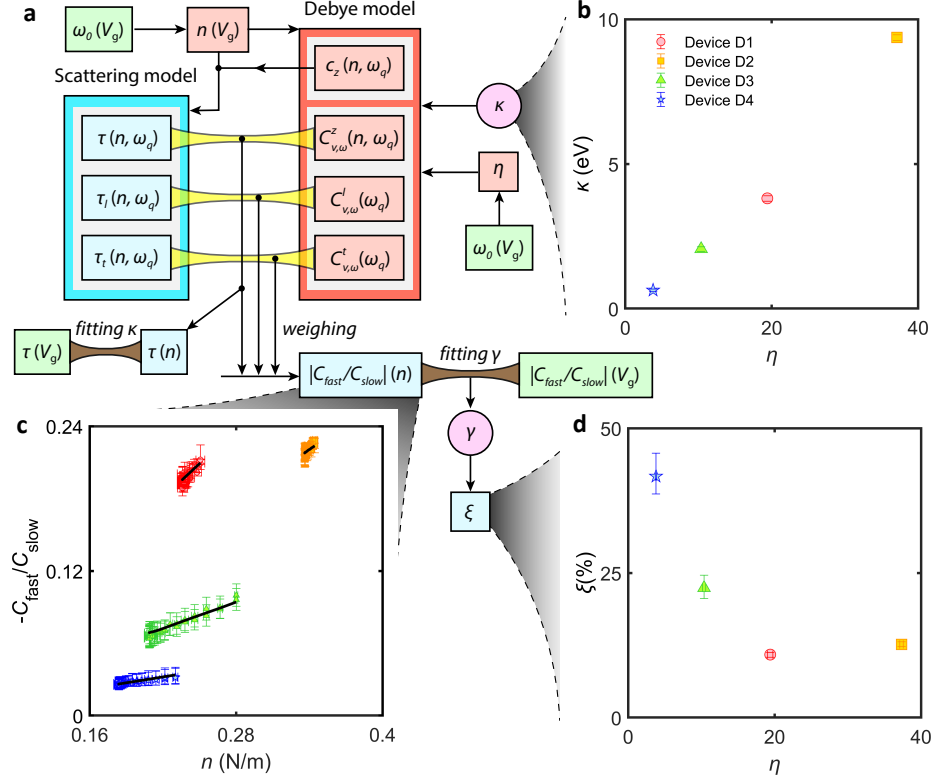


Fig. 3: Analysis and experimental demonstration on tunable heat transport in graphene drum devices. **a**, Flow chart of the theoretical model to estimate the thermal time constant τ and thermal expansion ratio $|C_{\text{fast}}/C_{\text{slow}}|$. Green frames: measured parameters; pink frames: fitting parameters. From Debye model we obtain the phonon frequency ω_q - dependent speed c_z and specific heats C_v^z , C_v^l , C_v^t for phonons, which are used as weighing factors in the scattering model to evaluate τ and $|C_{\text{fast}}/C_{\text{slow}}|$ as a function of tension n . **b**, Fitted bending rigidity κ of the membrane versus normalized areal mass η . These values of κ result in a good match between the modelled and measured τ for devices D1–D4, as plotted in Fig. 2b–2e (drawn lines). **c**, $|C_{\text{fast}}/C_{\text{slow}}|$ versus n . Points: the measurements; solid lines: the modelled estimates; error bars are from the fits to the thermal peaks. **d**, Percentual energy absorption ξ by flexural phonons as a function of η shows a strong decrease of ξ with increasing mass due to polymer residues.

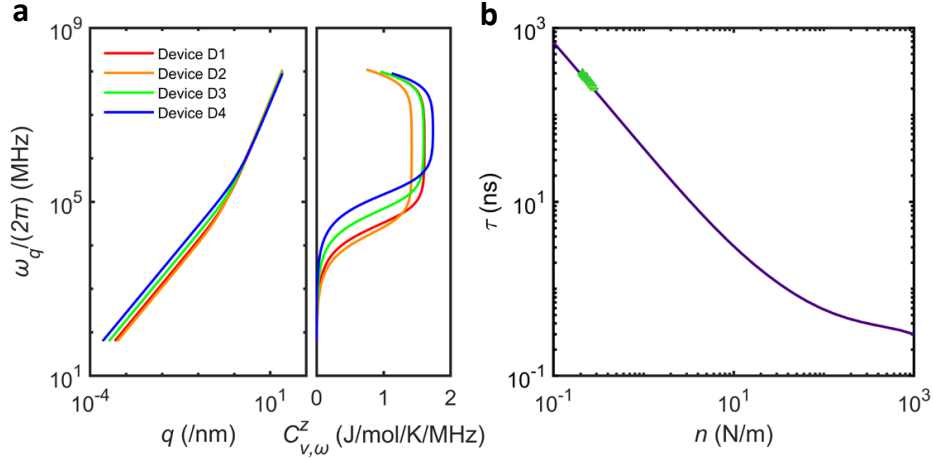


Fig. 4: Role of surface tension played on flexural phonons and tunability of heat transport rate in graphene membrane. **a**, Left panel: calculated dispersion relation of out-of-plane flexural phonons $\omega_q(q)$ for devices D1–D4, where the bending rigidity κ and normalized areal mass η are used from Table 1. $\omega_q(q)$ is dominated by tension n in \sim MHz regime and dominated by κ in \sim THz regime, respectively, while the cross-over frequency ω_{qc} is located at \sim GHz regime. Right panel: specific heat spectral density $C_{v,\omega}^z$ for all devices. **b**, Tunable thermal time constant τ with n varying from 0.1 to 1000 N/m, using device D3 as an example. Green points: measured τ versus n for device D3; solid line: estimated τ by Debye scattering model.

Supplementary Files

This is a list of supplementary files associated with this preprint. Click to download.

- [SupplementaryInformationHLiu.pdf](#)